Applied Thermal Engineering 232 (2023) 121039

Contents lists available at ScienceDirect

Applied Thermal Engineering

journal homepage: www.elsevier.com/locate/apthermeng

Research Paper

Dynamic behaviour of automobile thermoelectric waste heat recovery under different driving cycles

Ding Luo [a,c,*], Yuying Yan [d], Ying Li [d], Wei-Hsin Chen [e,f,g], Xuelin Yang [a], Xuehui Wang [b,*], Bingyang Cao [c,*]

[a] College of Electrical Engineering & New Energy, China Three Gorges University, Yichang 443000, China
[b] Chemical Engineering Department, Imperial College London, London SW7 2AZ, UK
[c] Key Laboratory for Thermal Science and Power Engineering of Ministry of Education, Department of Engineering Mechanics, Tsinghua University, Beijing 100084, China
[d] Faculty of Engineering, University of Nottingham, University Park, Nottingham NG7 2RD, UK
[e] Department of Aeronautics and Astronautics, National Cheng Kung University, Tainan 701, Taiwan
[f] Research Center for Smart Sustainable Circular Economy, Tunghai University, Taichung 407, Taiwan
[g] Department of Mechanical Engineering, National Chin-Yi University of Technology, Taichung 411, Taiwan

ARTICLE INFO

Keywords:
Thermoelectric generator
Dynamic behaviour
Waste heat recovery
Transient numerical model
Driving cycles

ABSTRACT

Different types of vehicles often run in different driving cycles, resulting in different dynamic behaviours of the automobile thermoelectric generator. The dynamic performance of a simplified automobile thermoelectric generator under different driving cycles, including HWFET, NEDC, WLTP, and CLTC, is evaluated to guide the application of automobile thermoelectric waste heat recovery by a hybrid transient CFD-TE model. The model is experimentally validated with an average output error of 10.92%, mainly caused by the instrument error. The findings indicate that the response of the dynamic output power of the automobile thermoelectric generator exhibits smoother fluctuations compared to the exhaust temperature, and also displays hysteresis in its response, while the dynamic conversion efficiency experiences sharp fluctuations. The behaviour of the automobile thermoelectric generator in dynamic situations is not entirely proportional to the vehicle speed but is instead dependent on changes in vehicle speed, more specifically, the change of exhaust heat. By comparing the steady and dynamic results, it is found that the steady-state model overestimates the output power but may underestimate the conversion efficiency. The automobile thermoelectric generator is more suitable for vehicles with frequent speed changes, such as passenger cars on urban and suburban roads, to enhance the dynamic output performance.

1. Introduction

Automobile exhaust heat recovery is one of the main applications of thermoelectric power generation technology. The automobile thermoelectric generator (ATEG) can convert exhaust heat into electricity and is typically positioned between the muffler and catalytic converter in a vehicle exhaust system [1]. The application prospect and feasibility of thermoelectric power generation in automobiles have been confirmed in previous studies through experimental tests [2,3] or theoretical analysis [4–6]. The exhaust heat is collected by a heat exchanger and then transferred to thermoelectric modules (TEMs), and a cooling device is applied to the cold side of TEMs to provide a cooling source. Driven by the temperature difference, the carriers in thermoelectric semiconductors move from the hot side to the cold side, thus generating electricity [7,8]. The power generation of the ATEG is contingent on the heat absorbed by the exhaust heat. The more heat the exhaust gas contains, the higher power the ATEG generates. In general, the vehicle is running under transient driving cycles, resulting in instantaneous changes in exhaust temperature and mass flow. Accordingly, the output power of the ATEG varies constantly with the fluctuation of exhaust heat.

Due to the complex dynamic characteristics of the ATEG, a great number of studies [9,10] have focused on the steady-state performance investigations of ATEGs. On the one hand, the exhaust gas under steady-state engine working conditions was often used as the heat source of the ATEG to study its energy recovery potential [11,12]. Bai et al. [13] investigated the performance of an ATEG with 72 TEMs through steady-

* Corresponding authors.
E-mail addresses: Ding_L@outlook.com (D. Luo), xuehui.wang@imperial.ac.uk (X. Wang), caoby@tsinghua.edu.cn (B. Cao).

https://doi.org/10.1016/j.applthermaleng.2023.121039
Received 3 April 2023; Received in revised form 31 May 2023; Accepted 20 June 2023
Available online 21 June 2023

Nomenclature

Symbols

c	specific heat capacity, $J{\cdot}kg^{-1}{\cdot}K^{-1}$
$\vec{E}$	electric field density vector, $V{\cdot}m^{-2}$
h	heat transfer coefficient, $W{\cdot}m^{-2}{\cdot}K^{-1}$
$\vec{J}$	current density vector, $A{\cdot}m^{-2}$
k	turbulent kinetic energy, $m^2{\cdot}s^{-2}$
$\dot{m}$	mass flow rate, $g{\cdot}s^{-1}$
p	pressure, Pa
P	output power, W
Q	heat, W
R	electrical resistance, Ω
t	time, s
T	temperature, K
U	output voltage, V
$\vec{v}$	Velocity, $m{\cdot}s^{-1}$

Greek symbols

ρ	density, $kg{\cdot}m^{-3}$
μ	dynamic viscosity, Pa·s
λ	thermal conductivity, $W{\cdot}m^{-1}{\cdot}K^{-1}$
α	Seebeck coefficient, $\mu V{\cdot}K^{-1}$
σ	electrical conductivity, $S{\cdot}m^{-1}$
σ^{-1}	electrical resistivity, Ω·m
ε	turbulent dissipation rate, $m^2{\cdot}s^{-3}$
η	conversion efficiency

Subscripts

c	cold side of the thermoelectric module
ce	ceramic materials
co	copper materials
ex	exhaust gas
exo	outlet surface of the exhaust channel
ext	external environment
h	hot side of the thermoelectric module
L	load resistance
n	n-type thermoelectric materials
p	p-type thermoelectric materials

Abbreviations

ATEG	Automobile thermoelectric generator
CFD	Computational fluid dynamics
CLTC	China Light-duty vehicle Test Cycle
HWFET	Highway Fuel Economy Test
NEDC	New European Driving Cycle
TE	Thermal-electric
TEM	Thermoelectric module
WLTP	Worldwide harmonized Light vehicles Test Procedure

state computational fluid dynamics (CFD) simulations. They reported that the output power of the ATEG can reach 323.42 W under the constant engine speed of 3000 r/min. To achieve a breakthrough of over 1000 W output power, Zhang [14] designed an ATEG with 400 TEMs and verified its performance through a steady-state engine test; The experimental results indicated that the ATEG could provide 1002.6 W electricity for an automobile diesel engine. On the other hand, to predict the overall performance of the ATEG under actual driving cycles, researchers [15,16] often took the average exhaust data under a complete driving cycle as boundary conditions to carry out performance analysis. Taking the average exhaust temperature and mass flow of the Federal Test Procedure (FTP-75) driving cycle as boundary conditions, Wang et al. [17] studied the influence of different parameters on the performance of the ATEG by using the proposed steady-state mathematical model. Similarly, taking the average exhaust data of the FTP driving cycle as boundary conditions of the CFD model, Nithyanandam and Mahajan [18] investigated the feasibility of using metal foam in the ATEG and declared that the metal foam could enhance the output performance. Automotive thermoelectric power generation has been proven to be a promising engine waste heat recovery technology.

Despite this, the steady-state performance analysis fails to uncover the ATEG's dynamic behaviour during transient driving cycles. The comparison between the steady-state performance and dynamic performance of the ATEG during the Economic Commission for Europe (ECE) driving cycles was conducted in Ref. [19], revealing that the steady-state analysis predicted an output 12.6% higher than the transient analysis. Therefore, it is more reasonable to study the dynamic behaviour of the ATEG. Crane et al. [20] integrated an ATEG into the exhaust system of a BMW six-cylinder engine and tested its performance under US06 drive cycles; The experimental results indicated that a maximum instantaneous power of over 500 W is reached. Similarly, Massaguer et al. [21] tested the energy recovery performance of an ATEG under the Worldwide harmonized Light vehicles Test Procedure (WLTP) and obtained that the energy generated by the ATEG in a complete driving cycle is 22.5 W•h. Risseh et al. [22] designed an ATEG for a heavy truck and tested its onboard performance under Long haulage driving cycles (LHC). The maximum instantaneous power output of the ATEG was determined to be around 1 kW based on the experimental results. It can be observed that there are a couple of experimental studies on the dynamic behaviour of the ATEG under driving cycles. However, the driving cycle used in different studies is various, and there is no comprehensive investigation and comparison of the dynamic behaviour of the ATEG under different driving cycles.

In the previous study [19], it was concluded that the ATEG exhibits response hysteresis in its dynamic output with changes in exhaust parameters, while short-term and minor fluctuations in exhaust gas have a negligible effect on its output performance. The dynamic behaviour of the ATEG varies greatly due to the substantial differences in the changing trends of exhaust mass flow rate and temperature across different driving cycles. The energy generated by the same ATEG under different driving cycles is various. It is crucial to explore the optimal driving cycle for guiding the application of the ATEG because different types of vehicles are usually driven in different driving cycles. For example, transport vehicles often run in highway driving conditions, while passenger cars often run in urban driving conditions. If the ATEG can generate higher energy gains under highway driving conditions, it is more suitable to be installed on transport vehicles. Due to the lack of reasonable transient models, researchers [23,24] mainly used experimental methods to study the dynamic behaviour of the ATEG. However, it is demanding and costly to carry out on-vehicle dynamic performance tests because the ATEG needs to be integrated into the vehicle, and the vehicle needs to be controlled to run accurately in specific driving cycles. The theoretical performance analysis for the dynamic behaviour of the ATEG is more feasible and profitable. Consequently, the hybrid transient CFD-thermal-electric (CFD-TE) numerical model first reported in the previous study [25] is used to predict the dynamic behaviour of the ATEG under different driving cycles. Compared with experimental methods, the given model can save execution time and cost. Compared with the reported transient analytical model [24], the given model considers dynamic characteristics and has higher accuracy.

In this work, a passenger car is set to run in four different driving cycles, including the New European Driving Cycle (NEDC), Highway Fuel Economy Test (HWFET), WLTP, and China Light-duty vehicle Test Cycle (CLTC). By using the transient exhaust mass flow rate and exhaust

temperature extracted from the exhaust gas as boundary conditions, a hybrid transient CFD-TE numerical model is employed to predict the dynamic behaviour of a simplified ATEG under various working conditions and to conduct a comprehensive analysis and comparison of the ATEG's dynamic performance across different driving cycles. Finally, some novel findings are highlighted, and some suggestions for the use of ATEG are disclosed. The findings presented in this paper aid in improving the understanding of the dynamic behaviour of the ATEG, and provide valuable guidance for its application.

2. Schematic of the automobile thermoelectric generator

To investigate the dynamic behaviour of the automobile thermoelectric generator (ATEG) under different driving cycles, a simplified ATEG is used as the research object, as shown in Fig. 1. The ATEG is comprised of a finned heat exchanger, a thermoelectric module (TEM), and a water-based cooling device. Here, only one TEM is included in the ATEG to reduce the workload and save computing resources and time. The simplified ATEG with only one TEM has the same dynamic behaviour as the ATEG with multiple TEMs. The aluminum heat exchanger is outfitted with a pair of steel connectors to allow for the ingress and egress of the exhaust gas. The cooling water flows through the aluminum cooling device to effectively remove the heat from the TEM. Electricity is produced by the TEM via the Seebeck effect, driven by the temperature difference. A Bi_2Te_3-based commercial TEM, manufactured by P&N Technology (Xiamen) Co., Ltd., is selected for the performance investigation. The used TEM includes 128 pairs of p-type and n-type thermoelectric legs ($1.4 \times 1.4 \times 1$ mm^3), 256 copper conducting strips ($1.4 \times 3.8 \times 0.35$ mm^3), and two Al_2O_3 ceramic plates (40×44 or 40×0.8 mm^3). Also, a load resistance ($35.5 \times 0.5 \times 0.5$ mm^3) is connected to the TEM to form a closed circuit. Detailed material properties of the ATEG are tabulated in Table 1, where the equivalent thermoelectric properties are determined using the experimental method outlined in Ref. [26]. The load resistance of 4 Ω is derived from the power optimization results in Ref. [27].

3. Model development and driving cycles

3.1. The hybrid transient CFD-TE model

The thermal-electric numerical model [28] is a common tool for assessing the output performance of thermoelectric generators, whereas the computational fluid dynamics (CFD) numerical model [29] is frequently employed to forecast the thermal distribution of thermoelectric systems. Most of the previous studies also follow this route. Since the ATEG consists of both the thermal-electric conversion of the TEM and the fluid flow of the exhaust gas and cooling water, a steady-state hybrid CFD-thermal-electric (CFD-TE) numerical model has been developed in recent research [30] to forecast the output performance of the ATEG by merging the thermal-electric numerical model with the CFD model. Due to the varying exhaust temperature and mass flow rate under different vehicle driving conditions, a steady-state model is not sufficient for predicting the dynamic behaviour of the ATEG when installed in the vehicle exhaust system. Therefore, a hybrid transient CFD-TE numerical model for the given ATEG has been established in the current study, in which the transient hot- and cold-side surface temperatures of the TEM, obtained from the transient CFD numerical model, are utilized as the transient boundary conditions of the transient thermal-electric numerical model. This model offers a significant reduction in computational time compared to the transient fluid-thermal-electric multiphysics numerical model discussed in Ref. [19]. In addition, according to the preliminary numerical calculation, it was found that the fluid-thermal-electric multiphysics numerical model suffers from the convergence problem, especially for the long-period driving cycle. Consequently, it is more feasible to use the hybrid transient CFD-TE numerical model to predict the dynamic behaviour of the ATEG under different driving cycles.

The hybrid transient CFD-TE numerical model is based on the following assumptions: i) Heat radiation is disregarded due to its negligible impact; ii) Isotropic thermoelectric materials are considered; iii) The material properties of dry air and water are assumed to represent the material properties of exhaust gas and coolant, respectively; iv)

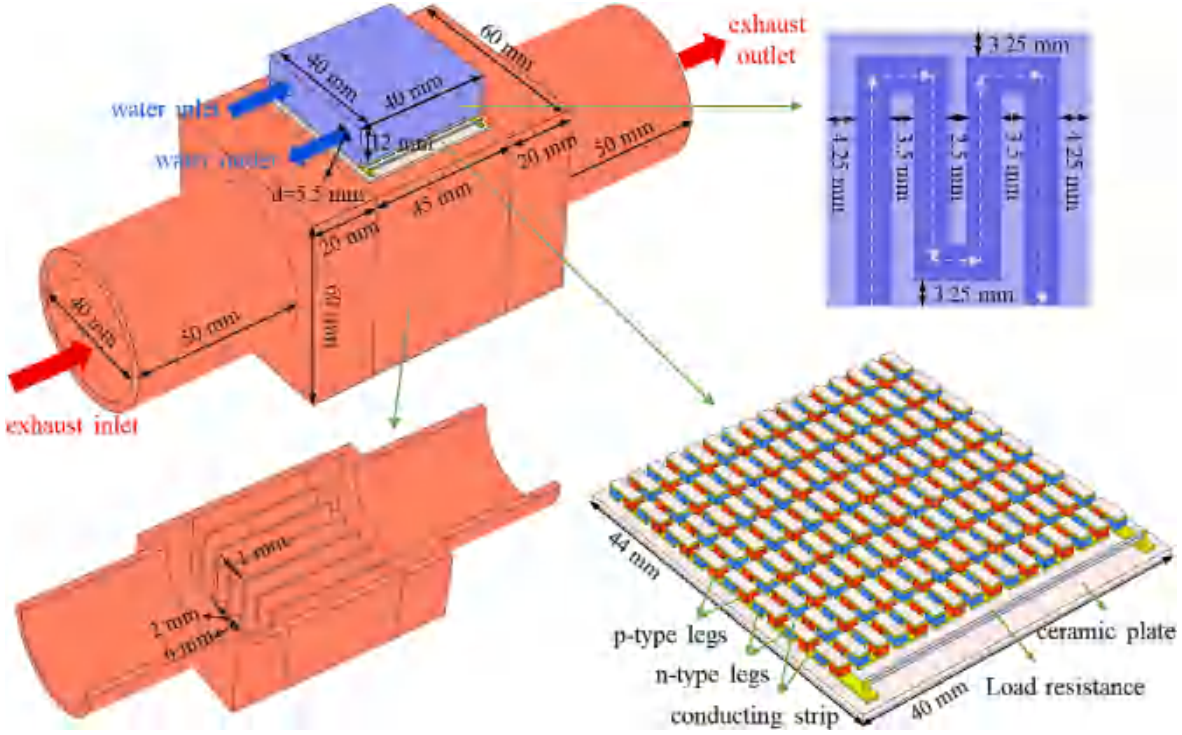

Fig. 1. Geometry of the automobile thermoelectric generator.

Table 1
Material properties of the ATEG.

Name	Parameter	Value	Unit
Aluminum heat exchanger and cooling device	Thermal conductivity	217.7	$W{\cdot}m^{-1}{\cdot}K^{-1}$
	Specific heat capacity	871	$J{\cdot}kg^{-1}{\cdot}K^{-1}$
	Density	2719	$kg{\cdot}m^{-3}$
Steel connectors	Thermal conductivity	17	$W{\cdot}m^{-1}{\cdot}K^{-1}$
	Specific heat capacity	502.48	$J{\cdot}kg^{-1}{\cdot}K^{-1}$
	Density	8030	$kg{\cdot}m^{-3}$
Al_2O_3 ceramic plates	Thermal conductivity	22	$W{\cdot}m^{-1}{\cdot}K^{-1}$
	Specific heat capacity	850	$J{\cdot}kg^{-1}{\cdot}K^{-1}$
	Density	3600	$kg{\cdot}m^{-3}$
Copper conducting strips	Thermal conductivity	165.64	$W{\cdot}m^{-1}{\cdot}K^{-1}$
	Specific heat capacity	381	$J{\cdot}kg^{-1}{\cdot}K^{-1}$
	Density	8978	$kg{\cdot}m^{-3}$
	Electrical resistivity	1.75×10^{-3}	$10^{-5}\ \Omega{\cdot}m$
Thermoelectric legs	p-type Seebeck coefficient	$-1.80268\times10^{-7}T^4+3.23632\times10^{-4}T^3-0.21537T^2+62.97444T-6616.56781$	$\mu V{\cdot}K^{-1}$
	n-type Seebeck coefficient	$1.80268\times10^{-7}T^4-3.23632\times10^{-4}T^3+0.21537T^2-62.97444T+6616.56781$	$\mu V{\cdot}K^{-1}$
	Thermal conductivity	$-3.0595\times10^{-9}T^4+4.5678\times10^{-6}T^3-2.5162\times10^{-3}T^2+0.6107T-53.9863$	$W{\cdot}m^{-1}{\cdot}K^{-1}$
	Electrical resistivity	$-3.088\times10^{-9}T^4+4.5653\times10^{-6}T^3-2.5854\times10^{-3}T^2+0.6558T-60.588$	$10^{-5}\ \Omega{\cdot}m$
	Specific heat capacity	188	$J{\cdot}kg^{-1}{\cdot}K^{-1}$
	Density	6600	$kg{\cdot}m^{-3}$
Load resistance	Electrical resistance	4	Ω
	Thermal conductivity	400	$W{\cdot}m^{-1}{\cdot}K^{-1}$
	Specific heat capacity	381	$J{\cdot}kg^{-1}{\cdot}K^{-1}$
	Density	8978	$kg{\cdot}m^{-3}$

Contact thermal resistance on both sides of the TEM is neglected due to its tiny influences [31]. Fig. 2 shows the schematic diagram of the hybrid transient CFD-TE numerical model. Mass, momentum, and energy conservations are expressed by Eqs (1)-(3) in the transient CFD numerical model. Eqs (4)-(5) are the transport equations of the standard k - ε turbulence model. The fluid flow and heat transfer in fluid zones can be characterized by Eqs (1)-(5) [32]. The transient energy balance equation can characterize the heat transfer in solid zones, as expressed in Eq. (6). Combined with reasonable boundary conditions, the governing equations (Eqs (1)-(6)) [32] of the transient CFD model can be solved by numerical methods.

The transient CFD results of the ATEG provide the transient hot- and

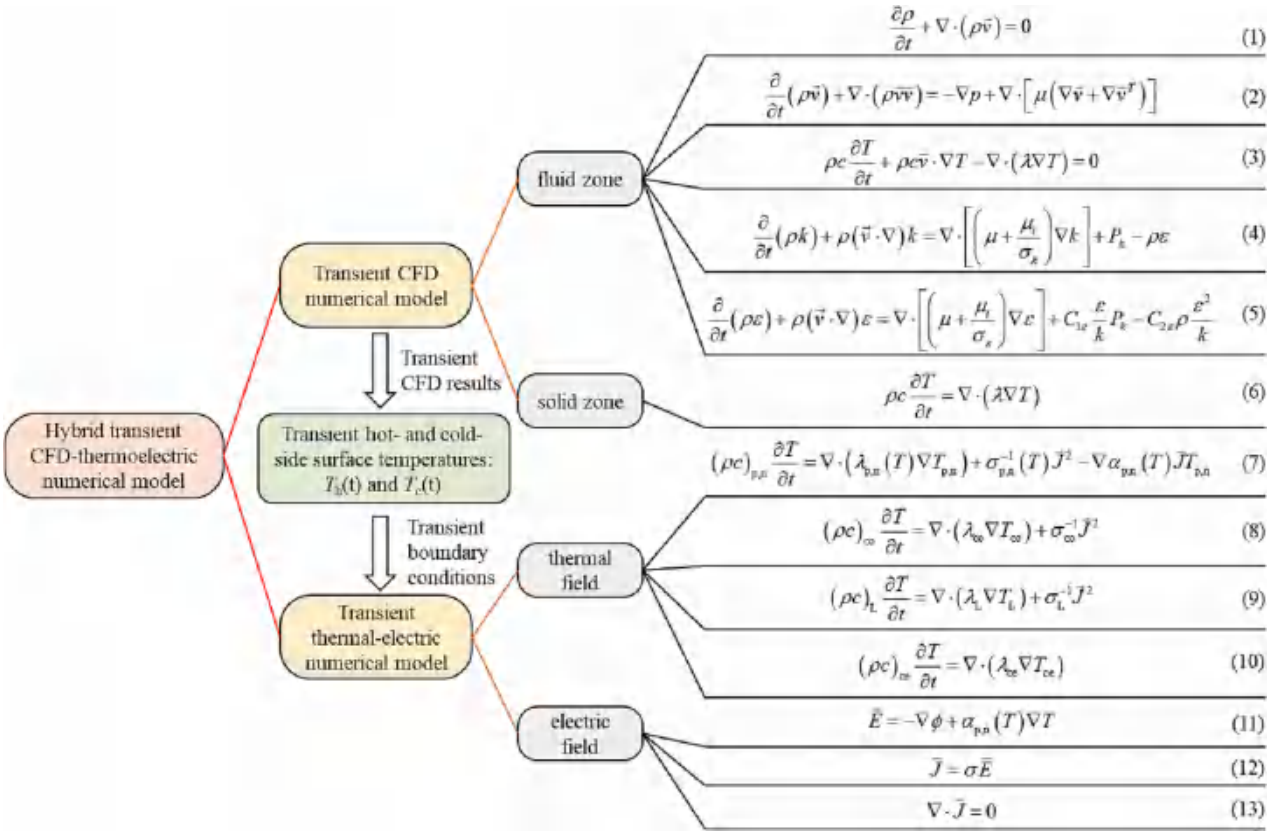

Fig. 2. Schematic diagram of the hybrid transient CFD-TE numerical model.

cold-side surface temperatures at both ends of the TEM, which are utilized as the transient boundary conditions of the transient thermal-electric numerical model to calculate the output performance of the TEM. Here, the transient thermal-electric numerical model includes the governing equations of the thermal and electric fields. Eqs (7) to (10) represent the transient energy conservation of thermoelectric legs, copper conducting strips, load resistance, and ceramic plates, respectively. In Eq. (7), the four terms from left to right represent the internal energy, Fourier heat, Joule heat, and Thomson heat in thermoelectric legs (or Peltier heat on the interfaces), respectively. The last term in Eq. (7) is absent in the transient energy conservation of copper conducting strips (Eq. (8)) and load resistance (Eq. (9)), due to the absence of the Seebeck effect. Also, ceramic plates are used for heat conduction and electric insulation. Therefore, only the internal energy and Fourier heat are included in the energy conservation equation, as expressed in Eq. (10). As for governing equations of the electric field, Eq. (11) gives the conservation of electrical potential, Eq. (12) gives the relationship between current density and electric field density, and Eq. (13) represents the continuity of current. More details about the variables can be found in Ref. [19].

3.2. Driving cycles

Considering the small cross-sectional area of the exhaust channel, the ATEG is adopted to recycle the exhaust heat of a passenger car. To obtain accurate exhaust data under different driving cycles, the vehicle type named VEH_SMCAR was selected as the application target in ADVISOR [33]. Other vehicle parameters that match this vehicle type were determined accordingly, as listed in Table 2. The passenger car was set to operate under four different driving cycles, including Highway Fuel Economy Test (HWFET), New European Driving Cycle (NEDC), Worldwide harmonized Light vehicles Test Procedure (WLTP), and China Light-duty vehicle Test Cycle (CLTC). HWFET is a high-speed driving cycle, which can stand for the vehicle's running condition on highway roads. NEDC is a driving cycle proposed by the European Union in 2000, which is world-widely used to evaluate the fuel economy of the vehicle on urban and suburban roads. WLTP is a more reasonable driving cycle to test the vehicle fuel economy released in 2014. In recent years, NEDC has been replaced by WLTP in many countries. CLTC is a driving cycle proposed by China to adapt to the driving conditions in China, which acts almost the same as WLTP. The periods of HWFET, NEDC, WLTP, and CLTC are 765 s, 1180 s, 1800 s, and 1800 s, respectively.

The corresponding exhaust mass flow rate and temperature along with the vehicle speed under different driving cycles are illustrated in Fig. 3. In general, the ATEG is installed between the muffler and the three-way catalytic converter of the vehicle exhaust system [34]. Therefore, when the vehicle reaches equilibrium, the exhaust temperature and exhaust mass flow rate are extracted from the corresponding exhaust data. It can be seen that the variation in vehicle speed will cause a change in exhaust mass flow rate and temperature. For example, the engine needs to burn more fossil fuels to produce more power to achieve the vehicle's acceleration, thus resulting in a higher exhaust mass flow rate and temperature, and vice versa. Compared with the severe fluctuation of exhaust mass flow rate, the change of exhaust temperature is more stable because the change of temperature is continuous and affected by thermal inertia. Also, the momentary fluctuation of the exhaust mass flow rate has a negligible impact on the exhaust temperature. The average vehicle speed, exhaust temperature, and exhaust mass flow rate under HWFET, NEDC, WLTP, and CLTC driving cycles are tabulated in Table 3. Through comparison, it is found that the exhaust temperature and mass flow rate fall within the reasonable range of experimental results in Ref. [5]. The average exhaust temperature under NEDC, WLTP, and CLTC is higher than that under HWFET, whereas the average exhaust mass flow rate under HWFET is the highest. It seems that the exhaust mass flow rate and temperature are not directly related to the vehicle speed. Even though the vehicle speed under HWFET is the highest, the output performance of the ATEG under HWFET may be lower than that under other driving cycles. More importantly, the instantaneous fluctuation of exhaust gas is quite different under different driving cycles, and the average values of exhaust mass flow rate and temperature can not directly reflect the output performance of the ATEG. It is crucial to study the dynamic behaviour of the ATEG under different driving cycles.

Table 2
Parameters of the selected passenger car in ADVISOR.

Parameter	Value	unit
Vehicle type	VEH_SMCAR	–
Engine type	FC_SI102_emis	–
Engine displacement	3	L
Number of cylinders	6	–
Cargo	200	kg
Total mass	1258	kg
Driving cycles	HWFET, NEDC, WLTP, CLTC	–

3.3. Boundary conditions and parameter definitions

As mentioned above, the hybrid transient CFD-TE numerical model comprises two submodels: the transient CFD numerical model and the transient TE numerical model. The boundary conditions of the transient CFD numerical model include the fluid region's inlet and outlet boundary conditions and the solid region's heat loss boundary conditions. The transient inlet boundary conditions of exhaust mass flow rate and temperature are defined on the inlet surface of the exhaust channel, and the steady inlet boundary conditions of water temperature and velocity are defined on the inlet surface of the water channel. For the outlet surfaces of the exhaust and the water channels, a pressure outlet boundary condition is adopted. In addition, the heat loss occurs on the surfaces of the ATEG exposed to the environment and is defined as follows:

$$-\lambda\frac{\partial T}{\partial n}=h_{\mathrm{ext}}(T-T_{\mathrm{ext}}) \tag{14}$$

where $h_{\mathrm{ext}}=15\ \mathrm{W\cdot m^{-2}\cdot K^{-1}}$ and $T_{\mathrm{ext}}=300\ \mathrm{K}$ [35] are respectively the external heat transfer coefficient and the external temperature.

Temperature and electric boundary conditions comprise the boundary conditions of the transient TE numerical model. Transient hot- and cold-side surface temperatures obtained from the CFD results serve as transient temperature boundary conditions. At the contact surface between the TEM and load resistance, close to the p-type leg, a grounded boundary condition is enforced. Comprehensive boundary conditions and values for the hybrid transient CFD-TE numerical model are listed in Table 4.

By numerical methods, the transient numerical results of the ATEG can be obtained based on the governing equations and boundary conditions of the hybrid transient CFD-TE numerical model. In this work, the numerical calculation of the ATEG is performed using the finite element method on the platform COMSOL [36]. The transient surface temperature and output voltage can be extracted from the obtained numerical results. Then, the transient output power of the ATEG is defined as [37]:

$$P(t)=\frac{U_{\mathrm{L}}^2(t)}{R_{\mathrm{L}}} \tag{15}$$

where $U_{\mathrm{L}}(t)$ is the transient output voltage of the ATEG.

The heat-to-electricity energy conversion efficiency is also a key index to estimate the behaviour of the ATEG, which can be estimated by [37]:

$$\eta(t)=\frac{P(t)}{Q_{\mathrm{h}}(t)}=\frac{P(t)}{c_{\mathrm{ex}}\dot{m}_{\mathrm{ex}}(t)[T_{\mathrm{ex}}(t)-T_{\mathrm{exo}}(t)]} \tag{16}$$

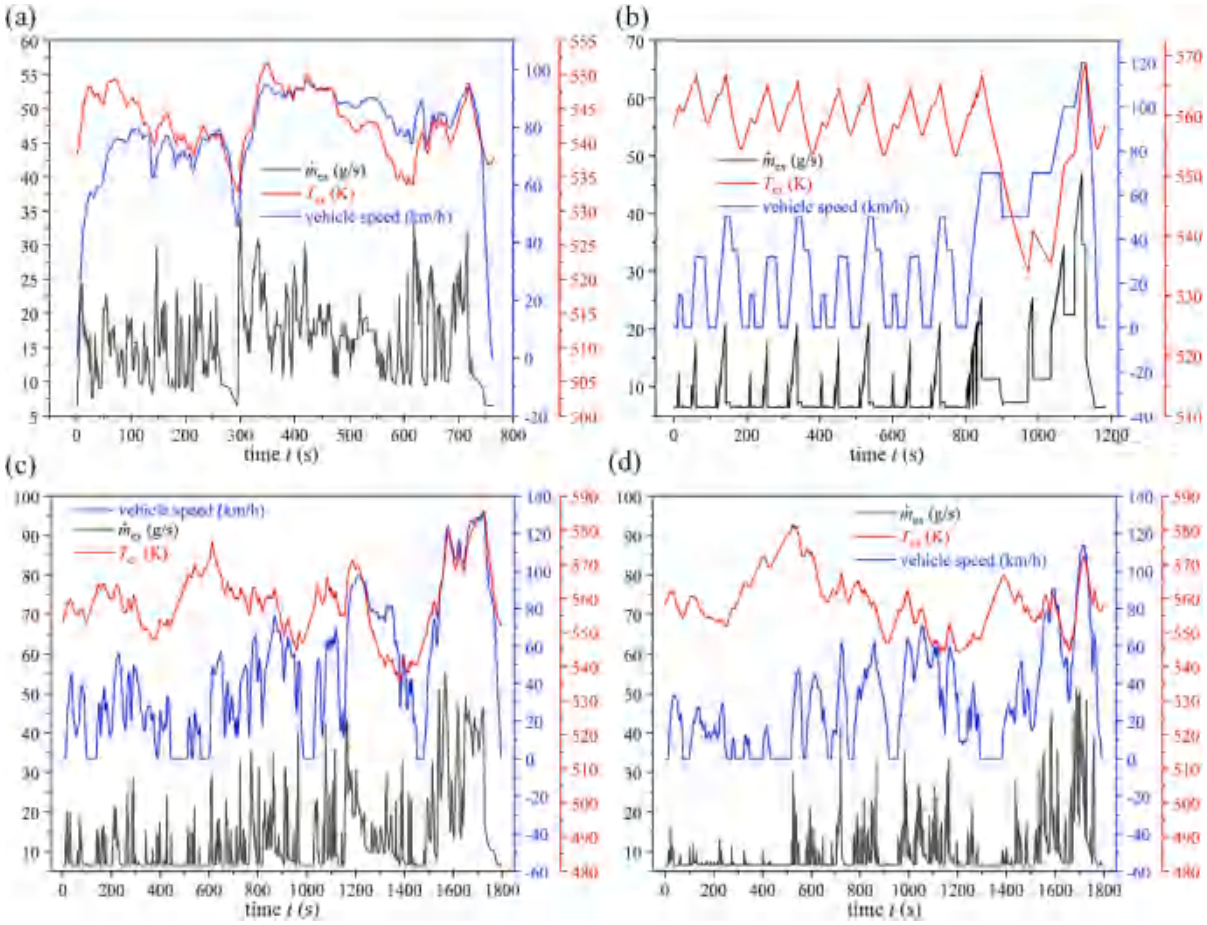

Fig. 3. Transient exhaust mass flow rate and temperature under different driving cycles. (a) HWFET; (b) NEDC; (C) WLTP; (d) CLTC.

Table 3
Average vehicle speed, exhaust temperature and flow rates under different drive cycles.

Driving cycles	Vehicle speed (km/h)	Exhaust temperature (K)	Exhaust mass flow rate (g/s)
HWFET	77.67	543.09	15.84
NEDC	33.24	557.03	10.25
WLTP	46.54	558.81	13.72
CLTC	28.97	558.97	9.92

where, c_{ex} is the specific heat capacity of the exhaust gas, and $T_{exo}(t)$ is the transient exhaust outlet temperature on the outlet surface of the exhaust channel.

3.4. Grid analysis

During the finite element simulation, the grid parameters play an important role in the accuracy of the model. The higher the grid quality, the higher the accuracy of model results. The grid of the ATEG is created by the specified physical fields to provide sufficient model accuracy. On the edge of fluid regions, for instance, the boundary layer grid with five layers is formed, and the grid at the corners is refined. Besides, the smaller the grid size is, the more accurate the model results are, but it requires more computing resources and time, and vice versa. To select a reasonable grid size, four grid strategies, i.e., 195,023 for the coarse grid, 454,702 for the normal grid, 1,505,248 for the fine grid, and 5,645,539 for the finer grid, are used for grid analysis. The initial numerical results show that the fine grid can not only maintain relatively

Table 4
Boundary conditions of the hybrid transient CFD-TE numerical model.

Submodel name	Boundary type	Position	Value	Unit
transient CFD numerical model	exhaust temperature inlet	inlet surface of the exhaust channel	$T_{ex}(t)$ in Fig. 3	K
	exhaust mass flow inlet	inlet surface of the exhaust channel	$\dot{m}_{ex}(t)$ in Fig. 3	g/s
	water temperature inlet	inlet surface of the water channel	300	K
	water velocity inlet	inlet surface of the water channel	1	m/s
	pressure outlet	outlet surfaces of the exhaust and water channels	101.325	kPa
	heat loss	surfaces of the ATEG exposed to the environment	Eq. (14)	–
transient TE numerical model	hot-side temperature	hot-side surface of the TEM	$T_h(t)$ from CFD results	K
	cold-side temperature	cold-side surface of the TEM	$T_c(t)$ from CFD results	K
	grounded boundary	contact surface between the TEM and load resistor near the p-type leg	0	V

high accuracy but also require less computing resources and time. Consequently, the fine grid with 1,505,248 grids is used for the following simulations.

4. Model validation

To verify the hybrid transient CFD-TE numerical model experimentally, a transient performance test bench of the ATEG was designed, as shown in Fig. 4. An air heater was used to generate high-temperature air for the ATEG. The transient heat source was generated by adjusting the temperature and flow knobs on the air heater. A temperature sensor was implemented at the inlet of the ATEG to measure the intake temperature, and a temperature data logger recorded the transient temperature data. Besides, a velocity sensor was placed behind the ATEG to measure the intake velocity, and a velocity data logger recorded the corresponding velocity data. Nevertheless, the operating temperature of the velocity sensor can not surpass 50 ℃. To protect the sensor, an air cooler was employed between the ATEG and the velocity sensor, powered by a DC power supply. For the cold side of the ATEG, tap water flowed through the cooling device to provide a cooling source, and its mass flow rate and temperature were 21.19 g/s and 284.85 K, respectively. Driven by the temperature difference, the TEM generated electricity and was connected with an electronic load (the load resistance was fixed at 4 Ω) to form a closed loop. The transient output voltage was captured using a voltage data recorder that was connected to the electronic load. Detailed apparatus information can be found in Table 5.

The transient output voltage of the ATEG obtained by this model is compared with experimental results, as well as the transient output voltage predicted by the transient fluid-thermal-electric numerical model [19], as shown in Fig. 5. As mentioned in Section 3.1, the transient fluid-thermal-electric multiphysics numerical model proposed in [19] suffers from the convergence problem, especially for the long-period driving cycle, even though it features high accuracy. Here, the transient output voltage of this model is compared with that of the previous model to figure out the difference between them. The measured air temperature and velocity in Fig. 5 are adopted as the boundary conditions of the hybrid transient CFD-TE numerical model and the transient fluid-thermal-electric multiphysics numerical model. It can be obtained that the output of the ATEG predicted by the hybrid transient CFD-TE numerical model is slightly higher than that predicted by the transient fluid-thermal-electric multiphysics numerical model. The fluctuation of experimental voltage is more obvious than model results, and the average voltage errors of the hybrid transient CFD-TE numerical model and the transient fluid-thermal-electric multiphysics numerical model are 10.92% and 9.24%, respectively. One of the reasons is the instrument error. Another reason is that the thermal inertia during the test can not be considered in the numerical calculation. Due to thermal inertia, the temperature sensor cannot react instantly when the ambient temperature changes, and the boundary temperature input of the models uses the measured temperature of the temperature sensor. The hybrid transient CFD-TE numerical model is capable of predicting the dynamic behaviour of the ATEG with an acceptable error for transient experiments. Compared with the transient fluid-thermal-electric multiphysics numerical model, this model can save computing time and resources, and the numerical calculation is easier to converge, only sacrificing less than 2% accuracy.

Table 5
Apparatus information of the transient performance test bench.

Name	Type	Manufacture	Key parameters
air heater	F1-R1055	FTV, China	maximum power: 5 kW
temperature sensor	K-type	Huarun, China	–
temperature data logger	RDXL4SD	OMEGA, US	accuracy: ± 0.4%
DC power supply	UTP1305	UNI-T, China	–
electronic load	IT8500+	ITECH, China	accuracy: ± 0.025%
voltage data logger	KSF	Keshun, China	accuracy: ± 0.2%
velocity sensor	HHF-SD1	OMEGA, US	–
velocity data logger	HHF-SD1	OMEGA, US	accuracy: ± 5%

5. Results and discussion

5.1. Contours of the ATEG obtained by the hybrid transient CFD-TE numerical model

Fig. 6 shows the temperature distributions of the ATEG at different time points under different driving cycles. The temperature of the heat exchanger drops as the exhaust gas descends. Also, the heat exchanger temperature is much greater at $t = 500$ s than it is at $t = 700$ s due to thermal inertia, as can be shown in Fig. 6(a), despite the exhaust temperature and mass flow rate being lower at $t = 500$ s than those at $t = 700$ s. According to Fig. 3(a), when $t = 500$ s, the exhaust temperature is in a state of decreasing, whereas it is the opposite for $t = 700$ s. However, due to the effect of thermal inertia, the temperature of the heat exchanger will not respond immediately and will remain in the previous state for a very short time. A similar phenomenon can be found in Fig. 6 (b) (between $t = 250$ s and $t = 500$ s) and Fig. 6(d) (between $t = 400$ s and $t = 800$ s). Under different driving cycles, there is a time that the exhaust mass flow rate is the same ($\dot{m}_{ex} = 6.55$ g/s), such as $t = 100$ s

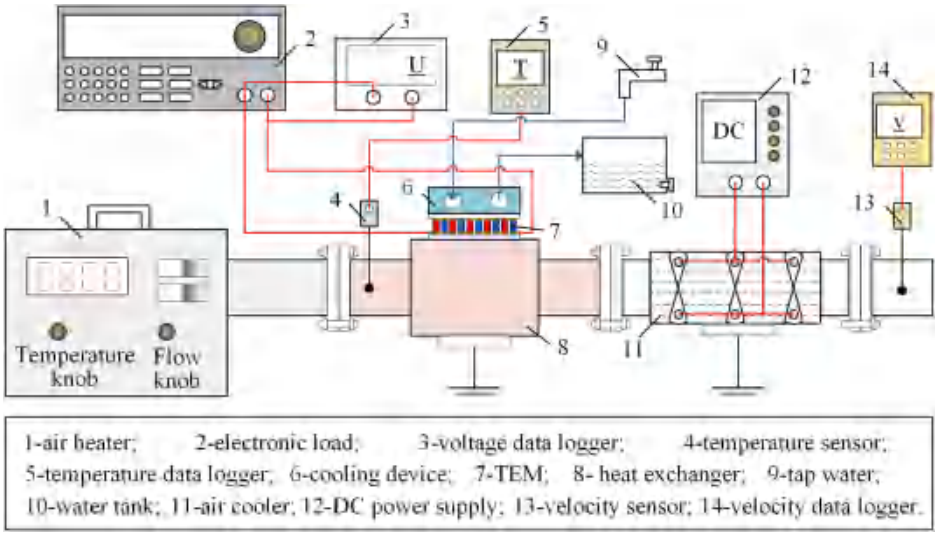

Fig. 4. Transient performance test rig of the ATEG.

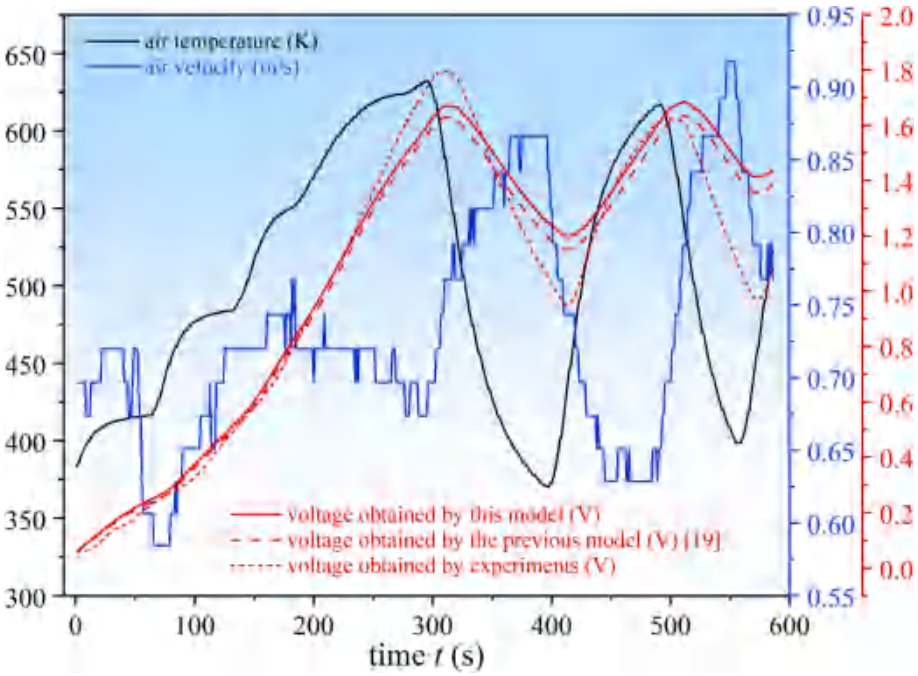

Fig. 5. Comparison of the transient output voltage of the ATEG between this model and experiments, as well as the previous model [19].

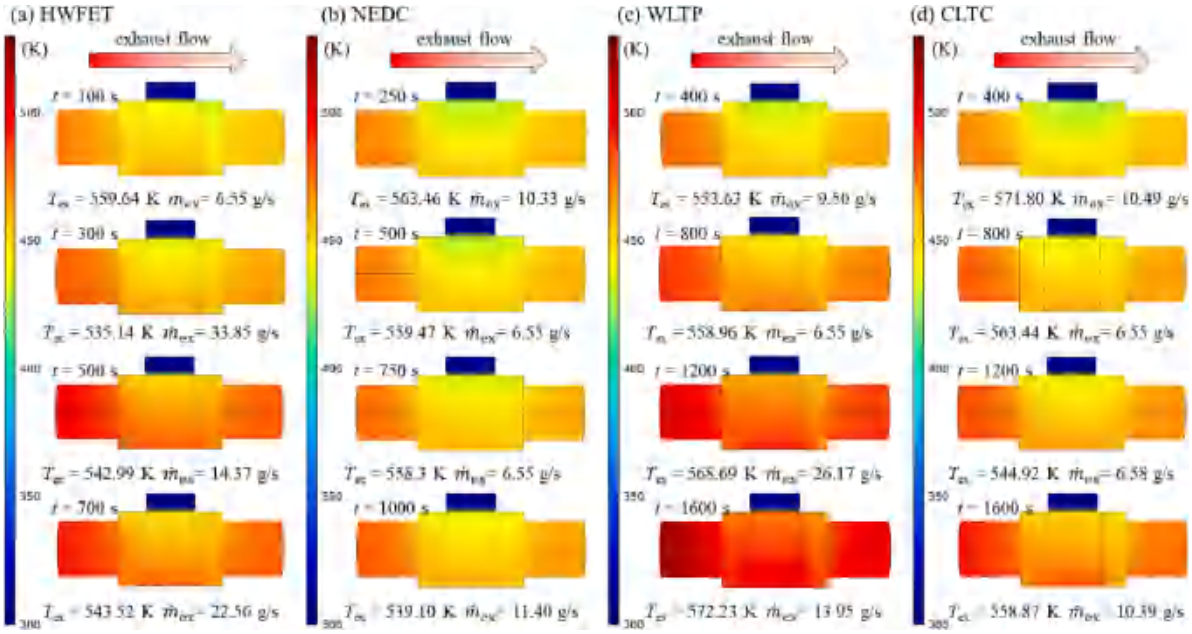

Fig. 6. Temperature distributions of the ATEG at different time points under different driving cycles. (a) HWFET; (b) NEDC; (c) WLTP; (d) CLTC.

under HWFET, $t = 500$ s and 750 s under NEDC, $t = 800$ s under WLTP, and $t = 800$ s under CLTC; even though the exhaust temperature is almost the same as that under HWFET and NEDC and lower than that under CLTC, the heat exchanger temperature under WLTP is the largest due to the thermal inertia. In general, it seems that the ATEG under WLTP enables the best thermal performance. However, the temperature distribution under several time points can not reflect the dynamic behaviour of the ATEG under a whole driving cycle. The global dynamic performance analysis of the ATEG under different driving cycles is performed in the following sections.

Fig. 7 shows the temperature distributions of the TEM at different time points under different driving cycles. Unlike the temperature distribution of the ATEG in Fig. 6, the TEM temperature distribution is directly related to the output performance of the ATEG. The temperature change of the hot side of the TEM is consistent with that of the heat exchanger in Fig. 6. However, the cold-side temperature is almost the same regardless of the change of exhaust mass flow rate and temperature due to the good cooling performance of the water-based cooling device. Therefore, the higher the hot-side temperature is, the larger the output power will be. Also, the hot-side temperature at $t = 1600$ s under WLTP ($T_h = 467.07$ K) is obviously higher than that at other time points, and the output performance will reach the maximum at this time point. The temperature of the load resistance is higher than that of other components because the Joule heat characterizes the power generated by the TEM.

The hybrid transient CFD-TE numerical model can predict the

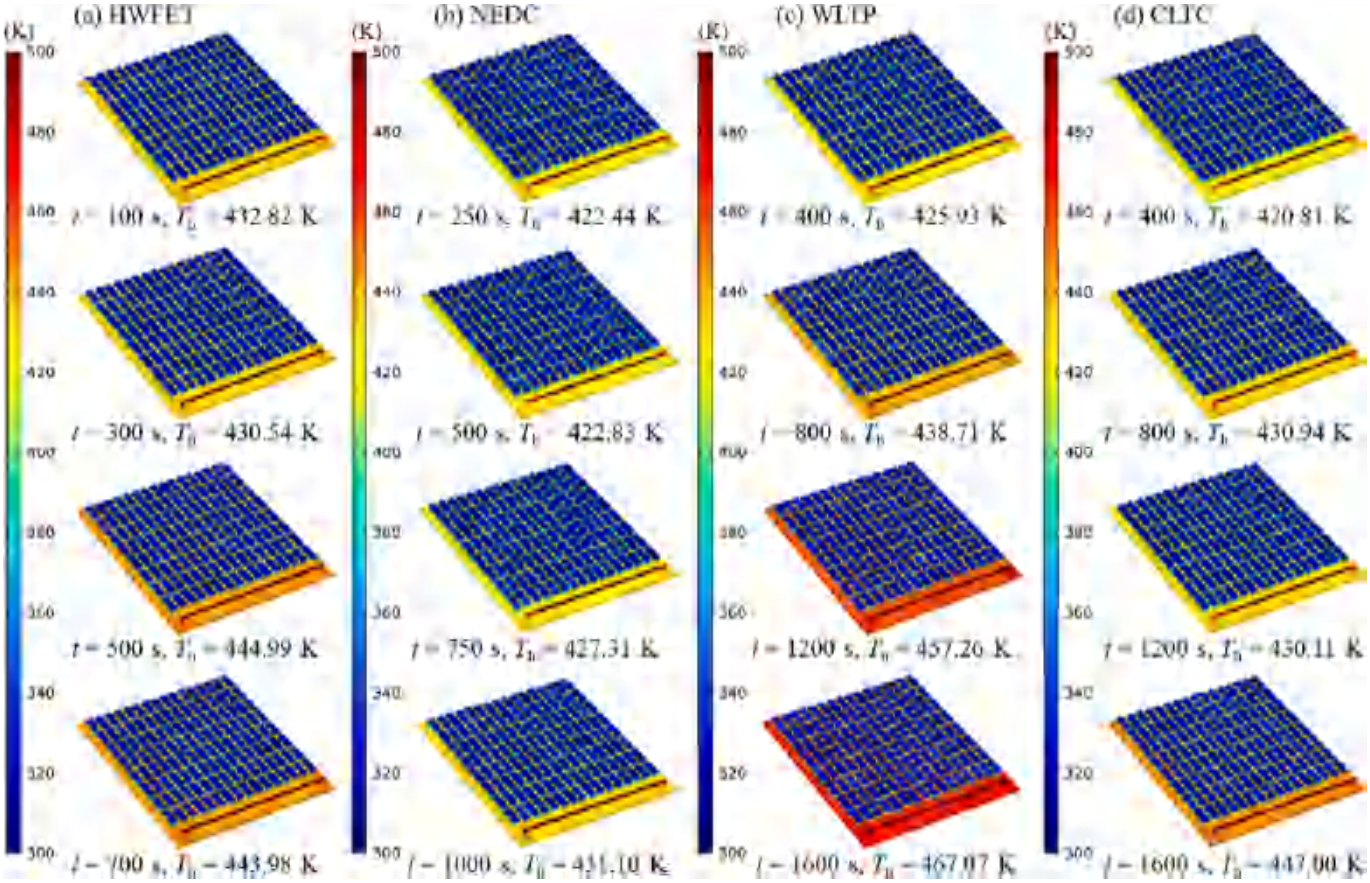

Fig. 7. Temperature distributions of the TEM at different time points under different driving cycles. (a) HWFET; (b) NEDC; (c) WLTP; (d) CLTC.

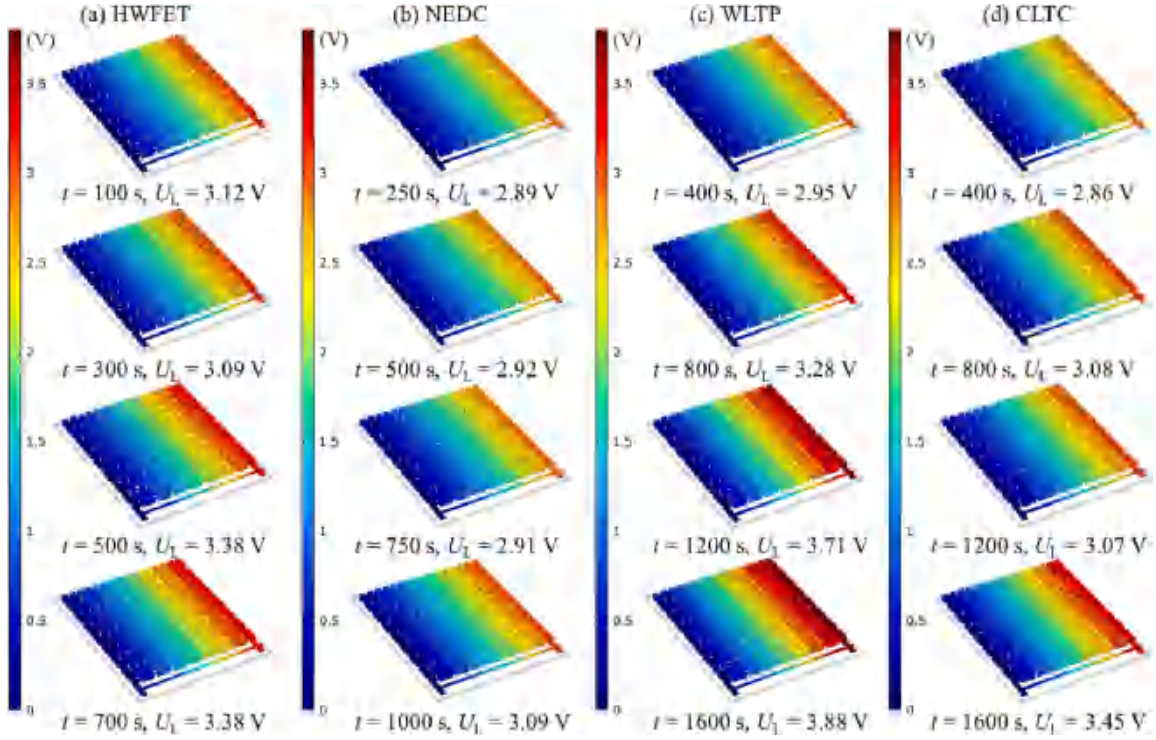

Fig. 8. Voltage distributions of the TEM at different time points under different driving cycles. (a) HWFET; (b) NEDC; (c) WLTP; (d) CLTC.

detailed voltage distribution of the TEM at any time point, as shown in Fig. 8. The electric potential of thermoelectric legs increases continuously from the terminal surface with the grounded boundary to the other terminal surface, and the electric potential difference of the load resistance is regarded as the output voltage of the TEM. The output voltage of the TEM is proportional to the temperature difference between the two sides. Consequently, the voltage change under different time points is consistent with the temperature change in Fig. 7, for example, under WLTP, when $t = 400$ s, 800 s, 1200 s, and 1600 s, the output voltage of the TEM is 2.95 V, 3.28 V, 3.71 V, and 3.88 V, corresponding to the hot-side temperature of 425.93 K, 438.71 K, 457.26 K, and 467.07 K, respectively. However, it can be noted that, compared with the huge response hysteresis in the heat transfer process from the exhaust gas to the heat exchanger, the response hysteresis in the heat transfer and heat-to-electricity conversion processes from the hot side of the TEM to thermoelectric legs is tiny, and the output voltage is almost synchronous with the hot-side temperature. The thermal inertia from the exhaust gas to the heat exchanger dominates the thermal inertia of the whole ATEG and contributes to the response delay of the output performance to a large extent. On the contrary, the thermal inertia of the exhaust heat can be fully utilized to improve the output performance of the ATEG, that is, when the hot-side temperature does not decrease because of the thermal inertia, the heating of the exhaust gas for the ATEG can be stopped until the temperature begins to decrease significantly. However, the transient change of the exhaust heat is quite different under different driving cycles. It is crucial to study the dynamic behaviour of the ATEG under different driving cycles to explore the best driving cycle and guide the application of the ATEG.

5.2. *Dynamic hot-side temperature and output power of the ATEG under different driving cycles*

The TEM's variation of the hot-side temperature can be extracted from the transient numerical results, as shown in Fig. 9. The hot-side temperature is proportional to the exhaust temperature and mass flow rate. From Fig. 9(a), the hot-side temperature shows a fluctuating increase from $t = 0$ s to $t = 260$ s, although the exhaust temperature only increases from $t = 0$ s to $t = 70$ s. The reason for the difference between the exhaust temperature and the hot-side temperature is that the heat exchanger is in the process of being continuously heated by the exhaust gas, and the exhaust mass flow rate shows a fluctuating increase. The temperature fluctuation is caused by the variation in the exhaust mass flow rate. Combined with the significant decrease of temperature from $t = 260$ s to $t = 300$ s, it can be noticed that the long-term decrease of the exhaust mass flow rate has a significant impact on the temperature, but the effect of the short-term fluctuation of the exhaust mass flow rate is tiny. Also, the time delay can be observed from the curve of the hot-side temperature, which can be explained by the thermal inertia in the heat transfer from the exhaust gas to the TEM. According to Fig. 9(b), the hot-side temperature curve is smoother than the exhaust temperature since there is a thermal buffering process in the transient heat transfer process. According to Fig. 9(c) and (d), the hot-side temperature remains a small change for a long time from $t = 450$ s to $t = 600$ s under WLTP and from $t = 0$ s to $t = 700$ s under CLTC, however, the exhaust temperature changes dramatically. The reason is that the exhaust mass flow rate does not fluctuate chronically and remains unchanged for a long time during these periods. The average hot-side temperatures under HWFET, NEDC, WLTP, and CLTC are 438.29 K, 428.53 K, 438.89 K, and 428.53 K,

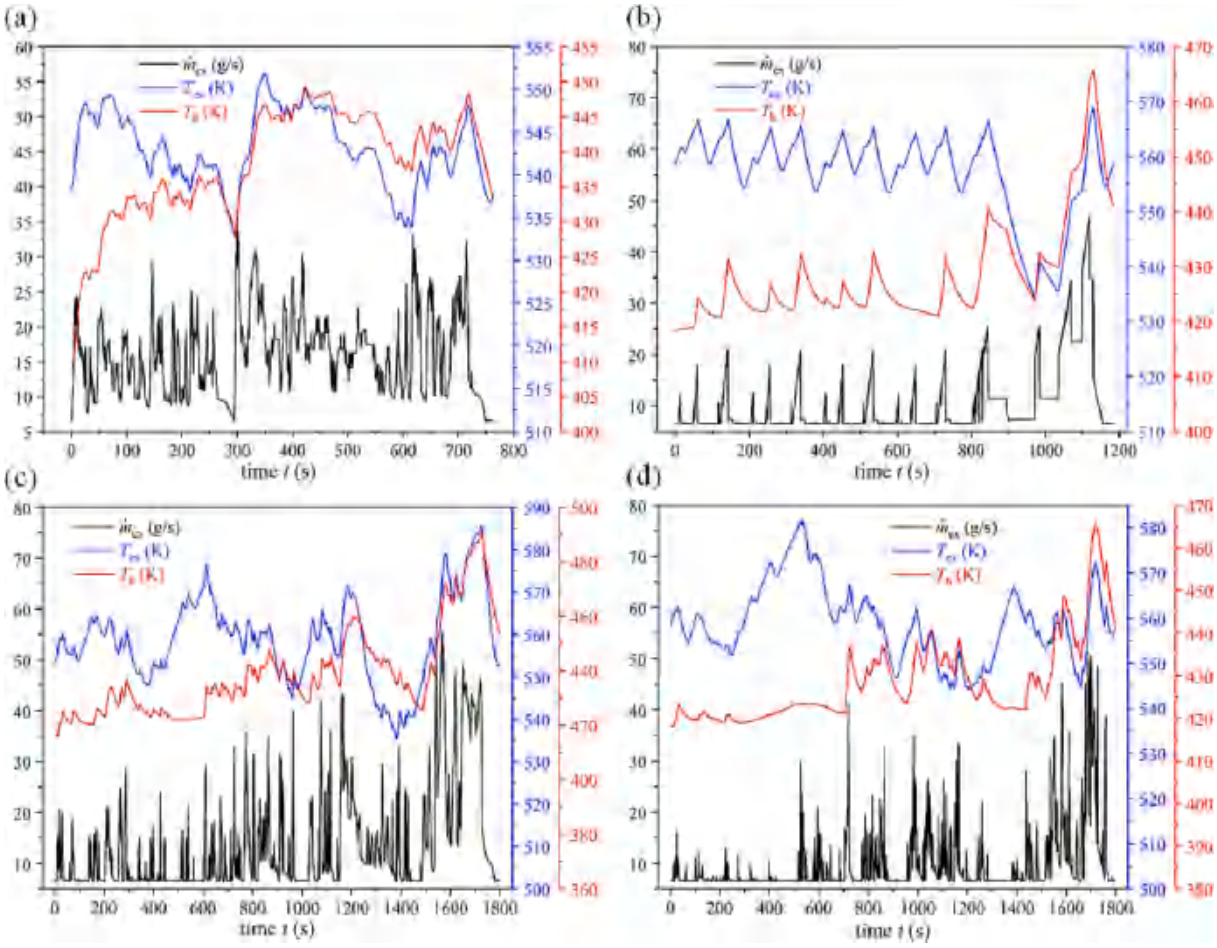

Fig. 9. Variation of the hot-side temperature of the TEM under different driving cycles. (a) HWFET; (b) NEDC; (c) WLTP; (d) CLTC.

respectively. In theory, the average output power of the ATEG under HWFET will be close to that under WLTP, and larger than that under NEDC and CLTC (the output power under NEDC should also be close to that under CLTC), because the transient hot-side temperature is directly adopted as the boundary condition of the transient TE numerical model to calculate the dynamic output of the TEM. Details about the output performance of the ATEG predicted by the transient model are discussed in the following sections.

Fig. 10 shows the variation of the output voltage and power of the ATEG under different driving cycles. The variation of output voltage and power is basically consistent with that of the hot-side temperature, but the change of output voltage and power is more stable, because the temperature input is smoothed by a continuous function in the internal solver of COMSOL, and the thermal inertia exists in the heat transfer from the hot-side of the TEM to thermoelectric legs. Also, the fluctuation of the output power curve is more obvious than that of the output voltage curve, because the output power is proportional to the square of the output voltage. The average output voltage of the ATEG under HWFET, NEDC, WLTP, and CLTC is 3.25 V, 3.03 V, 3.27 V, and 3.04 V, respectively, and the average output power of the ATEG is 2.65 W, 2.31 W, 2.70 W, and 2.32 W, respectively. The average output voltage and power under different driving cycles show the same results as the average hot-side temperature. Accordingly, the output power of the ATEG is the highest under WLTP, followed by HWFET; Under NEDC and CLTC, the output power of the ATEG is the same and the lowest. Consequently, the output performance of the ATEG is not directly related to the vehicle speed, even though the average vehicle under HWFET (77.67 km/h) is apparently than that under WLTP (46.54 km/h), the ATEG under WLTP can produce higher output performance. Compared with transport vehicles, the ATEG may be more suitable for waste heat recovery of passenger cars because the passenger car usually

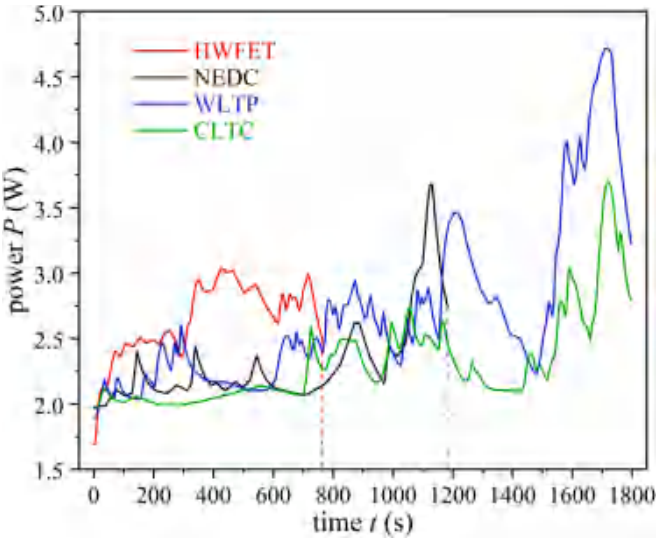

Fig. 11. Comparison of the transient output power of the ATEG under different driving cycles.

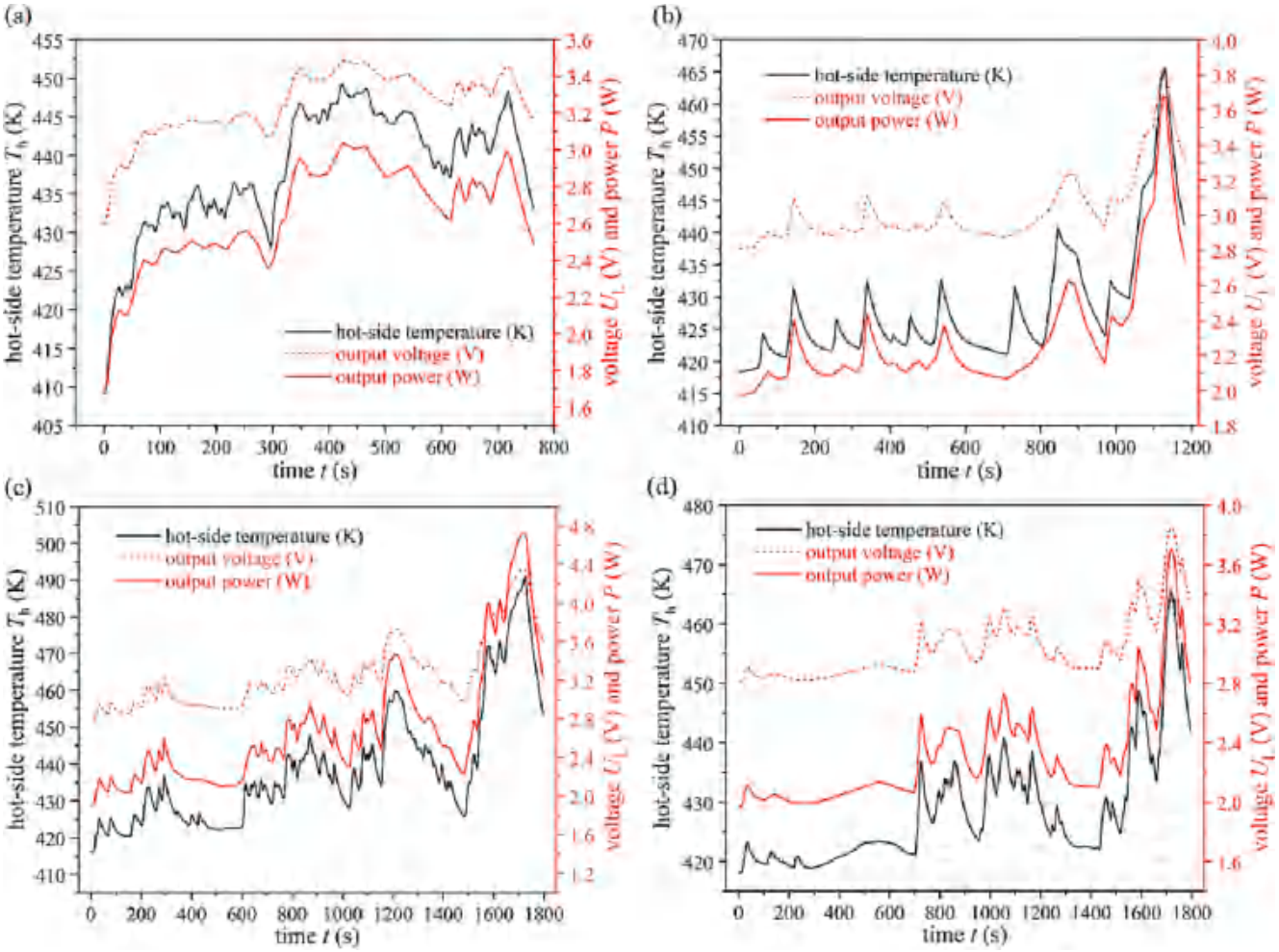

Fig. 10. Variation of the output voltage and power of the ATEG under different driving cycles. (a) HWFET; (b) NEDC; (c) WLTP; (d) CLTC.

operates under WLTP driving cycles, whereas the transport vehicle usually operates under HWFET driving cycles.

Fig. 11 compares the transient output power of the ATEG under different driving cycles. The maximum output power of the ATEG under HWFET, NEDC, WLTP, and CLTC is 3.04 W, 3.68 W, 4.72 W, and 3.70 W, respectively. The output power of the ATEG is relatively high under the whole HWFET driving cycle, and the power fluctuation is not obvious as in other driving cycles because the vehicle is always running at high speed under HWFET. The driving cycles of NEDC, WLTP, and CLTC consist of four-speed zones: low speed, medium speed, high speed, and ultra-high speed. Under the same driving cycle, the higher the vehicle speed is, the greater the output power of the ATEG will be. Combined with Fig. 3, it can be found that the ATEG can reach higher output performance when the vehicle speed fluctuates between medium and ultra-high speeds, instead of keeping a high speed all the time. Although the overall vehicle speed is higher when the vehicle remains at high speed all the time, the output power of the ATEG will be lower than that when the vehicle speed fluctuates between medium and ultra-high speeds. In addition, in practical application, the output power of the ATEG changes constantly, and thus it is crucial to develop an efficient energy recovery circuit [38] to recover the generated power.

5.3. Dynamic conversion efficiency of the ATEG under different driving cycles

The conversion efficiency of the ATEG is also an important index to assess its output performance, which is given by Eq. (16). In previous studies [39,40], the conversion efficiency of the ATEG under steady-state working conditions is generally lower than 2%. Nevertheless, the dynamic conversion efficiency may reach a higher value because the steady-state performance analysis underestimates the conversion efficiency of the ATEG [19]. Fig. 12 shows the variation in the heat absorption and conversion efficiency of the ATEG under different driving cycles. The change of heat absorption is almost the same as that of exhaust mass flow rate. The conversion efficiency curve can be viewed as the mirror of the curve of heat absorption because the conversion efficiency is inversely proportional to heat absorption. The maximum conversion efficiency of the ATEG under HWFET, NEDC, WLTP, and CLTC is 2.45%, 2.71%, 4.21%, and 2.72%, respectively. When the exhaust mass flow rate is reduced to a relatively low value, the heat absorption is also quite low. In contrast, the ATEG still generates electricity due to thermal inertia, resulting in ultra-high instantaneous conversion efficiency. However, the instantaneous conversion efficiency can not reflect the overall performance of the ATEG under the whole driving cycle. The average conversion efficiency of the ATEG under HWFET, NEDC, WLTP, and CLTC is 1.27%, 1.22%, 1.39%, and 1.23%, respectively. The ATEG under WLTP can produce the highest output power and the highest conversion efficiency. This is because the exhaust mass flow rate under WLTP frequently fluctuates between relatively high and low values, and the thermal inertia is fully utilized.

Fig. 13 compares the transient conversion efficiency of the ATEG under different driving cycles. As can be observed, the conversion efficiency under different driving cycles generally fluctuates around 1.2%. Combined with Figs. 3 and 12, the exhaust mass flow rate at idle speed is 6.55 g/s, but it does not decrease to 0, resulting in low heat absorption and high conversion efficiency at this time. It seems that if the exhaust

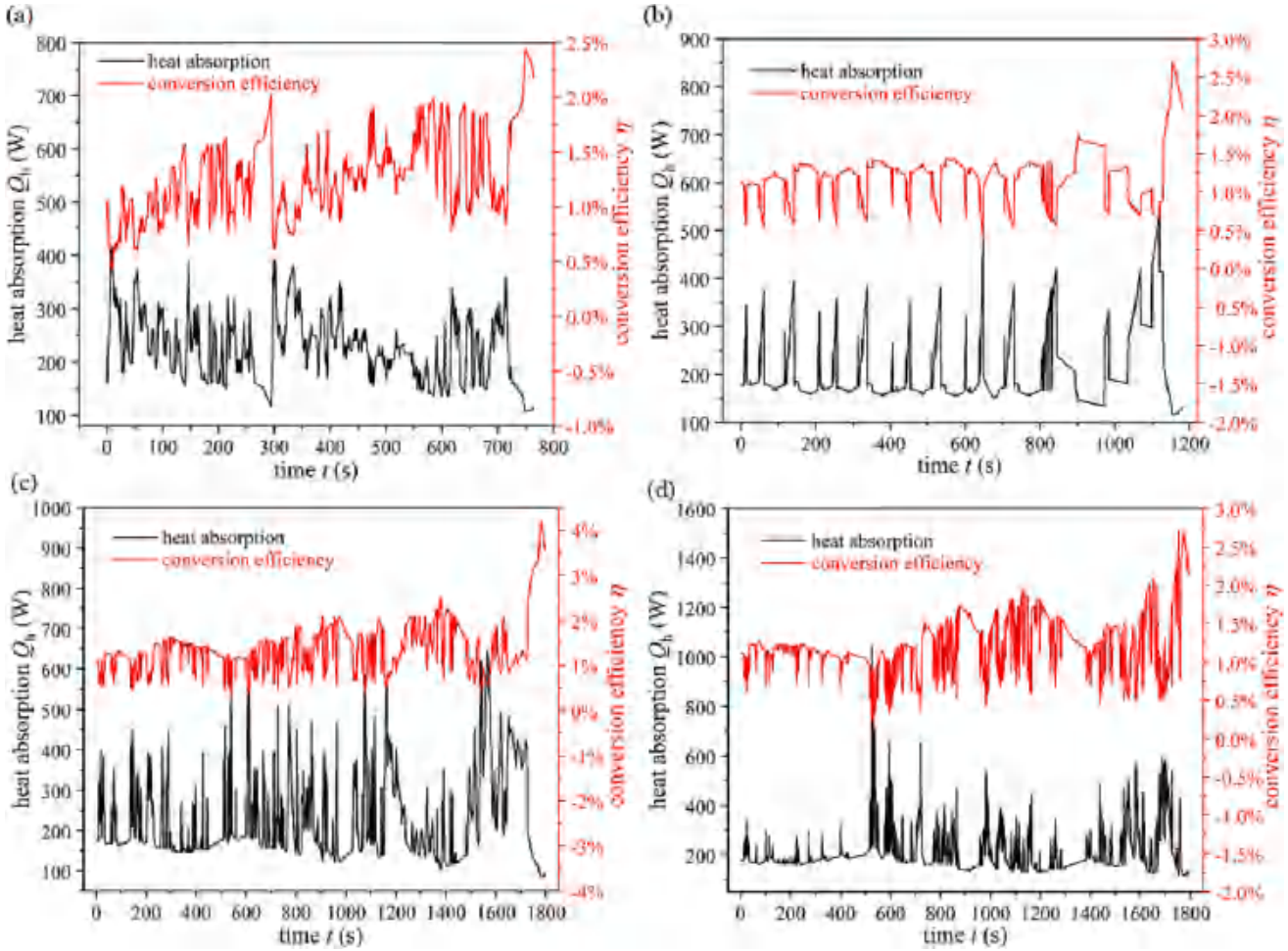

Fig. 12. Variation of the heat absorption and conversion efficiency of the ATEG under different driving cycles. (a) HWFET; (b) NEDC; (c) WLTP; (d) CLTC.

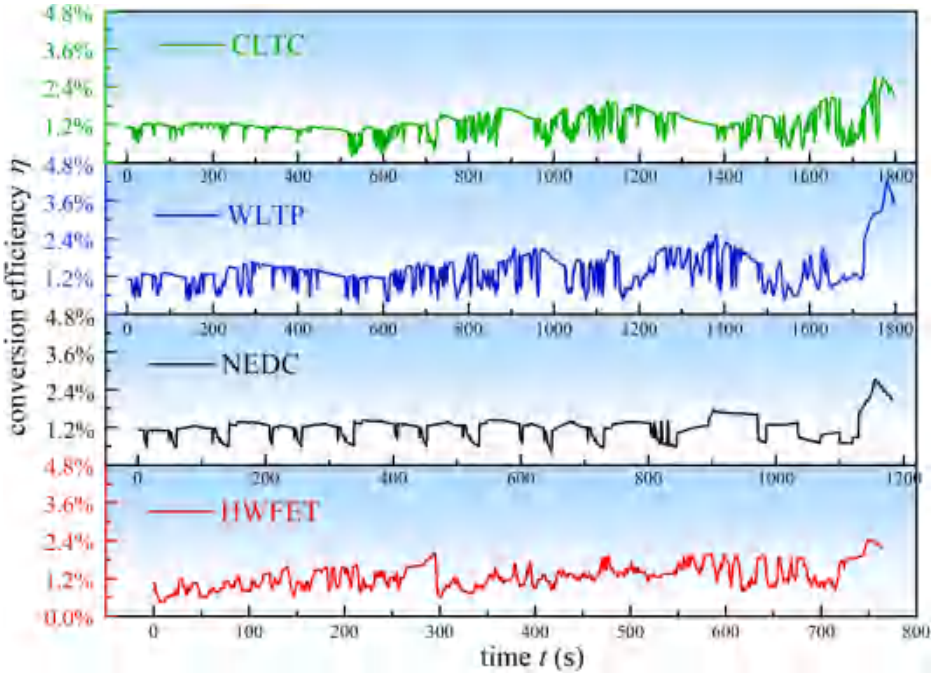

Fig. 13. Comparison of the transient conversion efficiency of the ATEG under different driving cycles.

mass flow rate at idle speed is reduced, the conversion efficiency can be further increased, and the intermittent heating of exhaust gas can improve the transient conversion efficiency more effectively. However, the vehicle will inevitably produce exhaust gas at idle speed. Besides the exhaust waste heat recovery in automobiles, thermoelectric generators can also be used in decentralized domestic power supply [41] and data center [42]. In this case, intermittent heating can be adopted to enhance heat-to-electricity energy conversion efficiency.

5.4. Comparison of average power and efficiency between transient and steady analysis

To analyze the difference between steady and transient performance analysis, the average output power and conversion efficiency predicted by the transient model under different driving cycles are compared with the steady output power and conversion efficiency predicted by the steady-state model, as shown in Fig. 14. Here, the steady-state performance of the ATEG is obtained by the hybrid steady-state CFD-TE numerical model using the average exhaust mass flow rate and temperature as boundary conditions. Under all driving cycles, the steady-state model overestimates the output power. The steady power is about 5.35%, 9.90%, 9.06%, and 8.93%, higher than the average power under HWFET, NEDC, WLTP, and CLTC, respectively. The steady efficiency is about 3.57%, 3.05%, and 2.28% higher than the average efficiency under HWFET, NEDC, and CLTC, respectively. However, the situation for WLTP is quite different, wherein the steady efficiency is 3.10% lower than the average efficiency, because the fluctuation of exhaust mass flow rate under WLTP is more frequent than that under other driving cycles. It can be concluded that the steady-state performance analysis overestimates the output power of the ATEG under practical driving cycles but may underestimate the conversion efficiency. In practical application, the frequent intermittent heating of exhaust gas can effectively improve the global conversion efficiency of the ATEG.

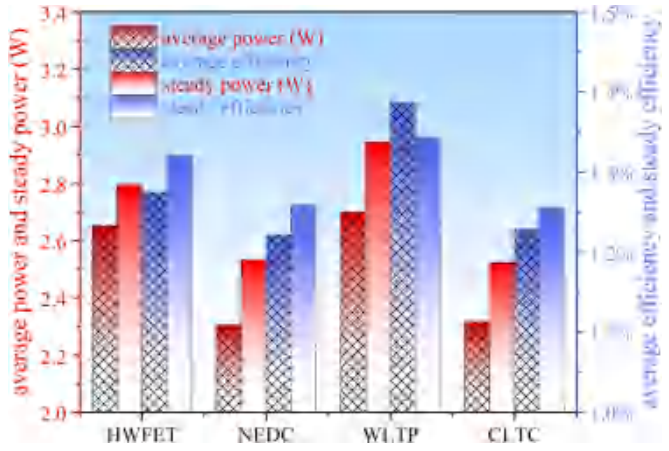

Fig. 14. Comparison of the overall output performance of the ATEG between steady and transient performance analysis.

6. Conclusions

In practical application, the output performance of the ATEG constantly fluctuates due to the instantaneous change of vehicle speed, and the energy profit is different under different driving cycles. This article uses a hybrid transient CFD-TE numerical model to predict the dynamic behaviour of the ATEG under four commonly used driving cycles, including HWFET, NEDC, WLTP, and CLTC. Taking the dynamic output power and conversion efficiency of the ATEG as the objective, the dynamic behaviour under different driving cycles is compared. Besides, to highlight the superiority of the dynamic performance analysis, the average output power and conversion efficiency predicted by the transient model are compared with the steady output power and conversion efficiency predicted by the steady-state model. According to the research results of this article, some novel findings are obtained as follows:

(1). The hybrid transient CFD-TE numerical model can be used to assess the dynamic behaviour of the ATEG under actual driving cycles and obtain the detailed temperature and voltage distributions of the ATEG at any time. Through transient experimental validation, the average error of output voltage between the experimental and model results is 10.92%, which is caused by the

instrument error and the underestimation of thermal inertia in the model.

(2). The dynamic performance of the ATEG is not completely proportional to the exhaust mass flow rate and temperature. Even though the exhaust heat is at a relatively low level, the dynamic output performance may be higher due to the thermal inertia in the heat transfer from the exhaust gas to the TEM. Compared with the transient fluctuation of exhaust temperature, the dynamic output power of the ATEG fluctuates more smoothly and features response hysteresis. However, the dynamic conversion efficiency of the ATEG fluctuates sharply, which can be regarded as the mirror curve of the exhaust mass flow rate.

(3). Under HWFET, NEDC, WLTP, and CLTC driving cycles, the average output power of the ATEG is 2.65 W, 2.31 W, 2.70 W, and 2.32 W, respectively, and the average conversion efficiency is 1.27%, 1.22%, 1.39%, and 1.23%, respectively. The ATEG enables the best dynamic performance under WLTP, followed by HWFET, CLTC, and NEDC. Even if the average vehicle speed is relatively high, the global output performance of the ATEG on highway roads may be lower than that on urban and suburban roads. The dynamic performance of the ATEG is not completely proportional to the vehicle speed but depends on the change of the vehicle speed, more specifically, the change of exhaust heat.

(4). Compared with dynamic performance analysis, the steady-state model overestimates the output power of the ATEG by 5.35%, 9.90%, 9.06%, and 8.93% under HWFET, NEDC, WLTP, and CLTC, respectively, and overestimates the conversion efficiency by 3.57%, 3.05%, and 2.28% under HWFET, NEDC, and CLTC, respectively, but underestimate the conversion efficiency by 3.10% under WLTP. The ATEG may be more suitable to be applied in vehicles with frequent speed changes because the exhaust heat fluctuates frequently and makes full use of the thermal inertia.

Declaration of Competing Interest

The authors declare that they have no known competing financial interests or personal relationships that could have appeared to influence the work reported in this paper.

Data availability

Data will be made available on request.

Acknowledgments

This work was supported by the National Key R&D Program of China (Grant No. 2022YFB3807700), the National Natural Science Foundation of China (52072217 and 22179071), and the Hubei Natural Science Foundation Innovation Group Project (2022CFA020).

References

[1] Z.-G. Shen, L.-L. Tian, X. Liu, Automotive exhaust thermoelectric generators: current status, challenges and future prospects, Energy Convers Manage 195 (2019) 1138–1173.
[2] T.Y. Kim, J. Kwak, B.-w. Kim, Energy harvesting performance of hexagonal shaped thermoelectric generator for passenger vehicle applications: an experimental approach. Energ. Convers Manage 160 (2018) 14–21.
[3] M. Ge, Z. Li, Y. Zhao, Z. Xuan, Y. Li, Y. Zhao, Experimental study of thermoelectric generator with different numbers of modules for waste heat recovery, Appl. Energ. 322 (2022), 119523.
[4] A. Massaguer, E. Massaguer, M. Comamala, T. Pujol, J.R. González, M.D. Cardenas, et al., A method to assess the fuel economy of automotive thermoelectric generators, Appl. Energy 222 (2018) 42–58.
[5] S. Lan, R. Stobart, R. Chen, Performance comparison of a thermoelectric generator applied in conventional vehicles and extended-range electric vehicles, Energy Convers Manage 266 (2022), 115791.
[6] Y. Zhao, M. Lu, Y. Li, Y. Wang, M. Ge, Numerical investigation of an exhaust thermoelectric generator with a perforated plate, Energy. 263 (2023), 125776.
[7] Y. Lou, G. Liu, A. Romagnoli, D. Ji, TEG-ORC combined cycle for geothermal source with coaxial casing well, Appl. Therm. Eng. 226 (2023), 120223.
[8] H. Cai, Z. Ye, G. Liu, A. Romagnoli, D. Ji, Sizing optimization of thermoelectric generator for low-grade thermal energy utilization: module level and system level, Appl. Therm. Eng. 221 (2023), 119823.
[9] A. Nour Eddine, D. Chalet, X. Faure, L. Aixala, P. Chessé, Effect of engine exhaust gas pulsations on the performance of a thermoelectric generator for wasted heat recovery: an experimental and analytical investigation, Energy. 162 (2018) 715–727.
[10] P. Fernández-Yáñez, O. Armas, R. Kiwan, A.G. Stefanopoulou, A.L. Boehman, A thermoelectric generator in exhaust systems of spark-ignition and compression-ignition engines. a comparison with an electric turbo-generator, Appl. Energy 229 (2018) 80–87.
[11] D. Luo, R. Wang, W. Yu, Z. Sun, X. Meng, Modelling and simulation study of a converging thermoelectric generator for engine waste heat recovery, Appl. Therm. Eng. 153 (2019) 837–847.
[12] D. Luo, Z. Sun, R. Wang, Performance investigation of a thermoelectric generator system applied in automobile exhaust waste heat recovery, Energy. 238 (2022), 121816.
[13] W. Bai, X. Yuan, X. Liu, Numerical investigation on the performances of automotive thermoelectric generator employing metal foam, Appl. Therm. Eng. 124 (2017) 178–184.
[14] Y. Zhang, Thermoelectric advances to Capture waste heat in automobiles, ACS Energy Lett. 3 (2018) 1523–1524.
[15] A.F. Agudelo, R. García-Contreras, J.R. Agudelo, O. Armas, Potential for exhaust gas energy recovery in a diesel passenger car under European driving cycle, Appl. Energy 174 (2016) 201–212.
[16] A. Massaguer, E. Massaguer, M. Comamala, T. Pujol, L. Montoro, M.D. Cardenas, et al., Transient behavior under a normalized driving cycle of an automotive thermoelectric generator, Appl. Energy 206 (2017) 1282–1296.
[17] Y. Wang, C. Dai, S. Wang, Theoretical analysis of a thermoelectric generator using exhaust gas of vehicles as heat source, Appl. Energy 112 (2013) 1171–1180.
[18] K. Nithyanandam, R.L. Mahajan, Evaluation of metal foam based thermoelectric generators for automobile waste heat recovery, Int. J. Heat Mass Transfer 122 (2018) 877–883.
[19] D. Luo, R. Wang, Y. Yan, W. Yu, W. Zhou, Transient numerical modelling of a thermoelectric generator system used for automotive exhaust waste heat recovery, Appl. Energy 297 (2021), 117151.
[20] D. Crane, J. LaGrandeur, V. Jovovic, M. Ranalli, M. Adldinger, E. Poliquin, et al., TEG On-vehicle performance and model validation and what it means for further TEG development, J. Electron Mater. 42 (2013) 1582–1591.
[21] A. Massaguer, T. Pujol, M. Comamala, E. Massaguer, Feasibility study on a vehicular thermoelectric generator coupled to an exhaust gas heater to improve aftertreatment's efficiency in cold-starts, Appl. Therm. Eng. 167 (2020), 114702.
[22] A.E. Risseh, H.-P. Nee, C. Goupil, Electrical power conditioning system for thermoelectric waste heat recovery in commercial vehicles, IEEE Trans. Transp. Electrification. 4 (2018) 548–562.
[23] S. Harish, D. Sivaprahasam, B. Jayachandran, R. Gopalan, G. Sundararajan, Performance of bismuth telluride modules under thermal cycling in an automotive exhaust thermoelectric generator, Energy Convers Manage 232 (2021), 113900.
[24] S. Lan, Z. Yang, R. Chen, R. Stobart, A dynamic model for thermoelectric generator applied to vehicle waste heat recovery, Appl. Energy 210 (2018) 327–338.
[25] D. Luo, Y. Yan, Y. Li, R. Wang, S. Cheng, X. Yang, et al., A hybrid transient CFD-thermoelectric numerical model for automobile thermoelectric generator systems, Appl. Energy 332 (2023), 120502.
[26] D. Luo, R. Wang, Experimental test and estimation of the equivalent thermoelectric properties for a thermoelectric module, J. Energy Res. Technol. 143 (2021), 122102.
[27] D. Luo, Y. Yan, R. Wang, W. Zhou, Numerical investigation on the dynamic response characteristics of a thermoelectric generator module under transient temperature excitations, Renew. Energy 170 (2021) 811–823.
[28] S. Shittu, G. Li, X. Zhao, X. Ma, Y.G. Akhlaghi, E. Ayodele, High performance and thermal stress analysis of a segmented annular thermoelectric generator, Energy Convers Manage 184 (2019) 180–193.
[29] X. Liu, C.-F. Zhang, J.-G. Zhou, X. Xiong, Y.-P. Wang, Thermal performance of battery thermal management system using fins to enhance the combination of thermoelectric Cooler and phase change Material, Appl. Energy 322 (2022), 119503.
[30] D. Luo, R. Wang, W. Yu, W. Zhou, A numerical study on the performance of a converging thermoelectric generator system used for waste heat recovery, Appl. Energy 270 (2020), 115181.
[31] S. Wang, T. Xie, H. Xie, Experimental study of the effects of the thermal contact resistance on the performance of thermoelectric generator, Appl. Therm. Eng. 130 (2018) 847–853.
[32] D. Luo, Z. Liu, Y. Yan, Y. Li, R. Wang, L. Zhang, et al., Recent advances in modeling and simulation of thermoelectric power generation, Energy Convers Manage 273 (2022), 116389.
[33] K.B. Wipke, M.R. Cuddy, S.D. Burch, ADVISOR 2.1: a user-friendly advanced powertrain simulation using a combined backward/forward approach, IEEE Trans. Veh. Technol. 48 (1999) 1751–1761.
[34] S. Twaha, J. Zhu, Y. Yan, B. Li, A comprehensive review of thermoelectric technology: materials, applications, modelling and performance improvement, Renew. Sustainable Energy Rev. 65 (2016) 698–726.
[35] D. Luo, R. Wang, W. Yu, W. Zhou, A novel optimization method for thermoelectric module used in waste heat recovery, Energy Convers Manage. 209 (2020), 112645.

[36] R.W. Pryor, Multiphysics modeling using COMSOL®: a first principles approach, Jones & Bartlett Publishers, 2009.
[37] D. Luo, Y. Yan, W.-H. Chen, X. Yang, H. Chen, B. Cao, et al., A comprehensive hybrid transient CFD-thermal resistance model for automobile thermoelectric generators, Int. J. Heat Mass Transfer 211 (2023), 124203.
[38] T.H. Kwan, X. Wu, The Lock-On Mechanism MPPT algorithm as applied to the hybrid photovoltaic cell and thermoelectric generator system, Appl. Energy 204 (2017) 873–886.
[39] H. Yang, G. Shu, H. Tian, X. Ma, T. Chen, P. Liu, Optimization of thermoelectric generator (TEG) integrated with three-way catalytic converter (TWC) for harvesting engine's exhaust waste heat, Appl. Therm. Eng. 144 (2018) 628–638.
[40] X. Lu, X. Yu, Z. Qu, Q. Wang, T. Ma, Experimental investigation on thermoelectric generator with non-uniform hot-side heat exchanger for waste heat recovery, Energy Convers Manage 150 (2017) 403–414.
[41] D. Champier, Thermoelectric generators: a review of applications, Energy Convers Manage 140 (2017) 167–181.
[42] W. He, J. Zhang, H. Li, R. Guo, S. Liu, X. Wu, et al., Effects of different water-cooled heat sinks on the cooling system performance in a data center, Energ. Buildings 292 (2023) 113162.